2024 IEEE 63rd Conference on Decision and Control (CDC)
December 16-19, 2024. MiCo, Milan, Italy

Motion Planning of 3D Nonholonomic Robots via Curvature-Constrained Vector Fields

Yike Qiao, Xiaodong He, and Zhongkui Li, *Senior Member, IEEE*

***Abstract*— Vector-field-based methods are typical feedback planning algorithms, especially eligible for the motion planning of nonholonomic robots. Nevertheless, most existing vector fields (VF) do not account for the prevalent constraints on robot's kinematics. This paper addresses the motion planning problem for 3D nonholonomic robots with trajectories featuring upper bounded curvature. To this end, a curvature-constrained VF over $\mathbb{R}^3$ is proposed, whose integral curves guarantee an upper-bound of curvature as well as an almost-global attraction region towards the desired position with a specified heading direction. Moreover, a control strategy is presented to determine the robot's control inputs subject to the curvature constraint. Under the designed control laws, the robot is guaranteed to track the VF while ensuring that the actual trajectory adheres to the curvature constraint. Finally, the efficacy of the presented motion planning algorithm is validated by numerical simulations.**

I. Introduction

Motion planning focuses on finding feasible paths or trajectories to guide a robot from its initial condition to the specified destination under certain constraints [1], [2]. Due to the physical interaction between robots and their environment, as well as the concern for motion capabilities of robots, nonholonomic constraint is prevalent in many robotic systems. In literature, it is customary to model a 3D nonholonomic robot as a 6-DOF rigid body with merely four control inputs, including a surge velocity and three angular velocity components [3], [4]. Nevertheless, physical limitations such as actuator saturation and maximum overload impose an upper bound on the curvature of robot's trajectory, leading to the curvature constraint in kinematics. As a result, both nonholonomic and curvature constraints have posed challenges to the application of existing motion planning methodologies.

Traditional motion planning approaches, such as the algorithms based on roadmap [5], cell decomposition [6] and sampling [7], usually neglect differential constraints to simplify the problem. Consequently, they cannot accommodate the nonholonomic constraint in kinematics. Although post-processing [8] and optimization [9] enable motion planning algorithms to address kinematic constraints, they are burdened by heavy computational demands. More importantly, these aforementioned methods are open-loop and require replanning when the system deviates significantly from the planned trajectories.

In the quest for feedback motion planning, scholars have investigated vector field (VF)-based approaches. VF is a map that assigns each point in workspace with a vector, specifying the desired velocity and the heading direction of nonholonomic robots simultaneously. Therefore, VF-based motion planning is naturally suitable to handle the nonholonomic constraint. The most common way to generate a VF is to calculate the gradient of an artificial potential field (APF) [10], [11], [12]. However, the implementation of the gradient-based vector field is challenging, stemming from the possible local minima in APF and the difficulty in constructing an APF free of local minima. To avoid the inherit drawbacks of APF, a handful of works design the VF in non-gradient ways [13], [14], [15], [16]. Despite those non-gradient-based VFs are easy to utilize and present almost global convergence, they do not consider the curvature constraint arising from the robot's kinematics. Consequently, curvature-constrained robots may not be able to follow these VFs, and hence fail to accomplish the motion task.

In order to handle the curvature constraint, Dubins car and Dubins curve are initially introduced in [17] and several curvature constrained path planning approaches are presented [18], [19]. Nonetheless, these algorithms, while considering both nonholonomic and curvature constraints, lack a feedback structure and thus are open-loop. To the knowledge of the authors, only a few papers integrate nonholonomic and curvature constraint into the framework of feedback motion planning. In [20], a gradient-based VF is proposed to generate trajectories satisfying curvature constraint. Authors in [21] present a local steering law for cruising UAV based on a parametric function to avoid collision under curvature constraint. Although [20], [21] are both closed-loop motion planning methods, they solely demonstrate the satisfaction of curvature constraint by tuning parameters in simulation results rather than theoretically analyzing the conditions to satisfy the curvature constraint.

In this paper, we propose a motion planning algorithm for 3D nonholonomic robots based on a non-gradient-based VF, where the robot is modeled as a 6-DOF rigid body with four control inputs and the curvature constraint is particularly taken into consideration. The contributions of this paper are twofold. Firstly, the workspace of the nonholonomic robot is elaborately divided into two regions so that the curvature

This work was supported in part by the National Science and Technology Major Project under grant 2022ZD0116401; in part by the National Natural Science Foundation of China under grants U2241214, 62373008, T2121002.
Corresponding author: Zhongkui Li.

Y. Qiao and Z. Li are with the State Key Laboratory for Turbulence and Complex Systems, Department of Mechanics and Engineering Science, College of Engineering, Peking University, Beijing 100871, China (e-mail: qiaoyike@stu.pku.edu.cn; zhongkli@pku.edu.cn)

X. He is with the School of Automation and Electrical Engineering, University of Science and Technology Beijing, Beijing 100083, China (e-mail: hxd@ustb.edu.cn)

979-8-3503-1632-2/24/$31.00 ©2024 IEEE

constrained VFs can be designed for each region separately. The integral curves (IC) of the proposed VF not only have an upper bounded curvature, but also are attracted from almost all initial conditions to the desired position along a specified tangent vector direction. Secondly, a control strategy is presented based on the VF with the curvature constraint. Under the proposed control laws, the robot is guaranteed to track the VF in a finite time and then move along the IC, such that it arrives at the desired position with a specified heading direction with an upper-bounded-curvature trajectory. Compared to our previous work [15], this paper further focuses on the crucial curvature constraint in the motion planning of nonholonomic robots, especially presenting novel VF and corresponding control laws, which guarantees the robot's trajectory is of bounded curvature.

The paper is organized as follows. Section II presents the 3D nonholonomic robot's kinematics and the problem formulation. The curvature-constrained VF and the control laws are proposed in Section III and IV, respectively. In Section V, numerical simulations are conducted to examine the efficacy of the proposed motion planning algorithm. Finally, Section VI provides the conclusion and future work.

II. Preliminaries and Problem Formulation

A. Nonholonomic Robots with Curvature Constraint

Consider a 6-DOF nonholonomic robot modelled as a rigid body. Let $\boldsymbol{\mathcal{F}}_i$ and $\boldsymbol{\mathcal{F}}_b$ denote the earth-fixed frame and the body-fixed frame, with canonical basis $\{\boldsymbol{e}_x^i, \boldsymbol{e}_y^i, \boldsymbol{e}_z^i\}$ and $\{\boldsymbol{e}_x^b, \boldsymbol{e}_y^b, \boldsymbol{e}_z^b\}$, respectively. The position of the robot in $\boldsymbol{\mathcal{F}}_i$ is specified by the position vector $\boldsymbol{p} = [x, y, z]^{\mathrm{T}}$, and the attitude is described by the rotation matrix $\boldsymbol{R} = [\boldsymbol{e}_x^b\ \boldsymbol{e}_y^b\ \boldsymbol{e}_z^b] \in \mathrm{SO}(3)$. For simplicity, the linear velocity $\boldsymbol{v} = [v_x, v_y, v_z]^{\mathrm{T}}$ and the angular velocity $\boldsymbol{\Omega} = [\Omega_x, \Omega_y, \Omega_z]^{\mathrm{T}}$ are provided in the body-fixed frame $\boldsymbol{\mathcal{F}}_b$. Then, the kinematics of the 3D rigid body robot can be given by

$$\dot{\boldsymbol{R}} = \boldsymbol{R}\boldsymbol{\Omega}^{\wedge}, \tag{1a}$$

$$\dot{\boldsymbol{p}} = \boldsymbol{R}\boldsymbol{v}, \tag{1b}$$

where the map $\wedge$ is defined by $(\boldsymbol{a}^{\wedge})\boldsymbol{b} = \boldsymbol{a} \times \boldsymbol{b}$, $\forall \boldsymbol{a}, \boldsymbol{b} \in \mathbb{R}^3$.

In this paper, we take into account both nonholonomic and curvature constraints on robot's kinematics. Owing to the nonholonomic constraint, the robot can only move along it's heading direction $\boldsymbol{e}_x^b$, implying $v_x \geqslant 0$, $v_y \equiv v_z \equiv 0$ and thereby

$$\dot{\boldsymbol{p}} = v_x \boldsymbol{e}_x^b. \tag{2}$$

Due to the physical limitations of the robot in real-world scenarios, the curvature of the robot's trajectory is usually bounded by a maximum curvature κ_{max}. In practice, the value of κ_{max} is easy to determine via experiments. Therefore, we assume that the maximum curvature κ_{max} is a known constant in the rest of this paper. By taking derivative of (2) and combining (1a), we can write the trajectory curvature of the nonholonomic robot as

$$\kappa = \frac{\sqrt{\Omega_y^2 + \Omega_z^2}}{v_x} \leqslant \kappa_{max}. \tag{3}$$

The aforementioned kinematics is a suitable modelling for a large number of realistic systems including fixed-wing UAV and autonomous underwater vehicles.

B. Problem Formulation

Motion Planning Problem: Consider a robot with kinematics given by (1)-(3). Let $\boldsymbol{p}_d$ and $\boldsymbol{e}_d$ denote the desired position and the heading direction in $\boldsymbol{\mathcal{F}}_i$, respectively. The objective of motion planning under consideration is to generate a trajectory $\boldsymbol{p}(t)$ of the nonholonomic robot by designing the linear velocity $\boldsymbol{v}(t)$ and the angular velocity $\boldsymbol{\Omega}(t)$ such that

$$\lim_{t\to\infty} \|\boldsymbol{p}(t) - \boldsymbol{p}_d\| = 0; \tag{4a}$$

$$\lim_{t\to\infty} \|\boldsymbol{e}_x^b(t) - \boldsymbol{e}_d\| = 0; \tag{4b}$$

$$\sqrt{\Omega_y^2 + \Omega_z^2}/v_x \leqslant \kappa_{max}, \forall t \geqslant 0. \tag{4c}$$

The above planning objectives require the robot to converge to the desired position denoted by (4a) with a curvature-bounded trajectory denoted by (4c), whose tangent vector points to the desired heading direction at the desired position denoted by (4b). Such a problem formulation is more challenging than simply guiding robots to certain positions as in [14] and [20], since nonholonomic robots cannot directly rotate to the desired heading direction while remaining at the desired position after the convergence of position.

III. Curvature-Constrained Vector Field

This section will present the non-gradient-based VF considering the curvature constraint. Compared with existing VFs, the proposed VF accounts for the curvature constraint and meanwhile exhibits almost global convergence since it does not suffer from local minima as those gradient-based ones.

Several relevant definitions are introduced in the following.

Definition 1. A vector field is a map $\mathbf{F}\colon \mathbb{R}^n \to \mathbb{R}^n$. Further, $\mathbf{F}$ is continuous if each component of $\mathbf{F}$ is continuous.

Definition 2. A singular point of the vector field is the point where $\mathbf{F}(\boldsymbol{p}) = \mathbf{0}$.

Definition 3. The integral curve $\mathcal{I}(t, \boldsymbol{p}_0)$ of a vector field $\mathbf{F}$ on $t \geqslant 0$ is the solution to $\dot{\boldsymbol{p}}(t) = \mathbf{F}(\boldsymbol{p}(t))$, $\boldsymbol{p}(0) = \boldsymbol{p}_0$.

Definition 4. A manifold $\mathcal{M} \subseteq \mathbb{R}^n$ is positively invariant w.r.t. $\mathbf{F}$ if $\boldsymbol{p}_0 \in \mathcal{M}$ implies $\mathcal{I}(t, \boldsymbol{p}_0) \in \mathcal{M}, \forall t \geqslant 0$.

We scheme to utilize the dipole-like VF inspired by [14] and [15], which is of desirable convergence properties, to navigate the robot. Nevertheless, the ICs of such a VF do not have bounded curvature in certain region. To this end, we divide the workspace $\mathbb{R}^3$ into two regions, so that we can redesign the curvature unbounded part of the dipole-like VF while keeping the part whose curvature is bounded. Firstly, we specify a set by

$$\mathcal{C} = \{\boldsymbol{p} \in \mathbb{R}^3 \mid x = 0, y^2 + z^2 = 4\rho^2\},$$

where $\rho = 1/\kappa_{max}$ is the minimum turning radius. The set $\mathcal{C}$ represents a circle in yOz plane of $\boldsymbol{\mathcal{F}}_i$ and is located at the origin with radius 2ρ. Next, the distance between a given point $\boldsymbol{p}$ and $\mathcal{C}$ is defined as $d_c(\boldsymbol{p}) = \sqrt{x^2 + (d_x - 2\rho)^2}$, where $d_x(\boldsymbol{p}) = \sqrt{y^2 + z^2}$ is the distance from $\boldsymbol{p}$ to the x-axis of $\boldsymbol{\mathcal{F}}_i$. In accordance with d_c, we divide the workspace $\mathbb{R}^3$ into the following two regions:

$$\mathcal{R}_1 = \left\{\boldsymbol{p} \in \mathbb{R}^3 \mid d_c < 2\rho\right\}, \tag{5}$$

$$\mathcal{R}_2 = \left\{\boldsymbol{p} \in \mathbb{R}^3 \mid d_c \geqslant 2\rho\right\}, \tag{6}$$

and design VF for each region respectively. Note that the region $\mathcal{R}_1$ is an open set of points whose distance to $\mathcal{C}$ is less than 2ρ, while $\mathcal{R}_2$ is the complementary set of $\mathcal{R}_1$ in $\mathbb{R}^3$.

By now, we are ready to propose the curvature-constrained VF. For $\boldsymbol{p} \in \mathcal{R}_1$, the redesigned VF is specified by

$$\mathbf{F}_1(\boldsymbol{p}) = \frac{1}{d_x}\begin{bmatrix} K d_x x - d_x^2 d_c + 2\rho d_x d_c \\ d_c x y + K d_x y - 2K\rho y \\ d_c x z + K d_x z - 2K\rho z \end{bmatrix}, \tag{7}$$

where $K = \sqrt{4\rho^2 - d_c^2}$. It should be noted that $d_x \neq 0$ in $\mathcal{R}_1$ and thus $\mathbf{F}_1$ is well defined. For $\boldsymbol{p} \in \mathcal{R}_2$, we employ the dipole-like VF in [15], which is given by

$$\mathbf{F}_2(\boldsymbol{p}) = \begin{bmatrix} x^2 - y^2 - z^2 \\ 2xy \\ 2xz \end{bmatrix}. \tag{8}$$

In order to generate a continuous VF over $\mathbb{R}^3$ except for singular points of $\mathbf{F}_i, i = 1, 2$, we normalize the VFs, i.e.,

$$\mathbf{F}(\boldsymbol{p}) = \begin{cases} \frac{\mathbf{F}_i}{\|\mathbf{F}_i\|}, & \|\mathbf{F}_i\| \neq 0, \\ \mathbf{0}, & \|\mathbf{F}_i\| = 0. \end{cases} \tag{9}$$

Let $\mathcal{S}_i$ denote the singular point set of $\mathbf{F}_i$. According to (7) and (8), we know that $\mathcal{S}_1 = \{\boldsymbol{p} \in \mathbb{R}^3 \mid d_c = 0\} = \mathcal{C}$ and $\mathcal{S}_2 = \{\boldsymbol{p} = \mathbf{0}\}$. Hence, the singular point set of $\mathbf{F}$ is given by $\mathcal{S} = \mathcal{S}_1 \bigcup \mathcal{S}_2$. The proposed VF is shown in Figure 1, where the ICs of VF are depicted by solid lines.

Lemma 1. *The plane defined by* $\Sigma_{ab} = \{\boldsymbol{p} \in \mathbb{R}^3 \mid ay + bz = 0, a^2 + b^2 \neq 0\}$ *is a positively invariant manifold w.r.t. the VF* $\mathbf{F}$ *proposed in* (9).

Proof. Denote the normal vector of Σ_{ab} as $\boldsymbol{n}_{ab} = [0, a, b]^{\mathrm{T}}$. Based on (7), (8) and (9), it can be shown that

$$\boldsymbol{n}_{ab} \cdot \boldsymbol{p} = 0,\ \boldsymbol{n}_{ab} \cdot \mathbf{F}(\boldsymbol{p}) = 0,\ \forall \boldsymbol{p} \in \Sigma_{ab}. \tag{10}$$

According to (10), for any $\boldsymbol{p} \in \Sigma_{ab}$, the corresponding vector $\mathbf{F}(\boldsymbol{p})$ is also confined in Σ_{ab}. Therefore, it is straightforward that the IC of $\mathbf{F}$ with $\boldsymbol{p}_0 \in \Sigma_{ab}$ is also confined in the Σ_{ab} and Σ_{ab} is an invariant manifold w.r.t. $\mathbf{F}$. □

Theorem 1. *Denote* $\chi_+ = \left\{\boldsymbol{p} \in \mathbb{R}^3 \mid x > 0, y = z = 0\right\}$, $\chi_- = \left\{\boldsymbol{p} \in \mathbb{R}^3 \mid x < 0, y = z = 0\right\}$ *and define the non-converging set* $\mathcal{N} = \chi_+ \bigcup \mathcal{S}$. *The VF* $\mathbf{F}$ *proposed in* (9) *has following properties:*

1) $\mathbf{F}$ *is continuous on* $\mathcal{D} = \mathbb{R}^3 \backslash \mathcal{S}$.

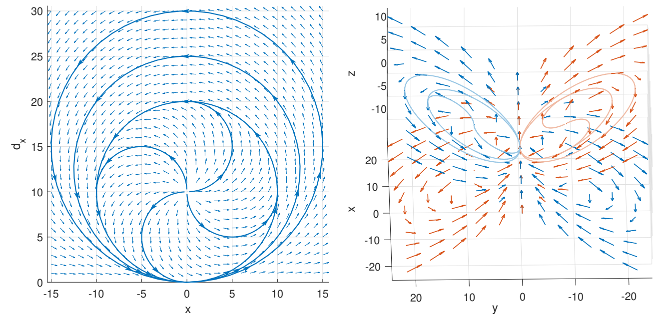

(a) In Σ_{ab} plane (b) In different Σ_{ab} planes

Fig. 1. Plots of the proposed VF $\mathbf{F}$ and its ICs, where VF and ICs are presented by arrows and solid curves respectively.

2) *For all initial conditions* $\boldsymbol{p}_0 \in \mathbb{R}^3 \backslash \mathcal{N}$, *the origin is attractive for the dynamics* $\dot{\boldsymbol{p}} = \mathbf{F}(\boldsymbol{p})$, *and the tangent vector of* $\mathcal{I}(t, \boldsymbol{p}_0)$ *coincides with* $\boldsymbol{e}_x^i$ *at the origin.*
3) *For all initial conditions* $\boldsymbol{p}_0 \in \mathbb{R}^3 \backslash \mathcal{S}$, *the curvature of* $\mathcal{I}(t, \boldsymbol{p}_0)$ *satisfies* $\kappa(t) \leqslant \kappa_{max}, \forall t \geqslant 0$.

Proof. 1) Referring to the continuity criteria in [22], we know that $\mathbf{F}$ is continuous on both $\mathcal{R}_1 \backslash \mathcal{S}_1$ and $\mathcal{R}_2 \backslash \mathcal{S}_2$. Therefore, $\mathbf{F}$ is continuous on $\mathcal{D} = \mathbb{R}^3 \backslash \mathcal{S}$ if it is continuous on $\partial\mathcal{R}_1 \backslash \mathcal{S}_2$, namely, the boundary between $\mathcal{R}_1$ and $\mathcal{R}_2$ excepting the singular point $\mathcal{S}_2$. The continuity on $\partial\mathcal{R}_1 \backslash \mathcal{S}_2$ could be proved by simple calculations and hence $\mathbf{F}$ is continuous over $\mathcal{D}$. However, the above discussions do not imply the smoothness of proposed VF.

2) The proof in this part can be divided into two cases, depending on the initial position $\boldsymbol{p}_0$.

• Case 1: $\boldsymbol{p}_0 \in \mathcal{R}_2 \backslash (\chi_+ \bigcup \mathcal{S}_2)$.

Since we utilize the dipole-like VF in $\mathcal{R}_2$, we can directly write the expressions of ICs in this case by carrying on time reparametrization (refer to [23]) on the ICs in [15, Theorem 1]. We begin with the trivial situation where $\boldsymbol{p}_0 \in \chi_-$. There is

$$\mathcal{I}(t, \boldsymbol{p}_0) = \begin{cases} [t + x_0, 0, 0]^{\mathrm{T}}, & 0 \leqslant t \leqslant t_f, \\ \mathbf{0}, & t > t_f, \end{cases} \tag{11}$$

where $t_f = -x_0$. Obviously, the tangent vector of such IC at the origin is $\boldsymbol{e}_x^i$.

For the general situation where $\boldsymbol{p}_0 \in \mathcal{R}_2 \backslash (\chi_- \bigcup \chi_+ \bigcup \mathcal{S}_2)$, consider the coordinates (r, ϕ, θ) transformed by

$$x = r\cos\phi, \tag{12a}$$

$$y = (r\sin\phi + r)\cos\theta, \tag{12b}$$

$$z = (r\sin\phi + r)\sin\theta. \tag{12c}$$

Then the IC for $\boldsymbol{p}_0 \in \mathcal{R}_2 \backslash (\chi_- \bigcup \chi_+ \bigcup \mathcal{S}_2)$ is given by

$$r(t) = r_0,\ \phi(t) = \frac{t}{r_0} + \phi_0,\ \theta(t) = \theta_0,\ \forall t \leqslant t_{f2}, \tag{13}$$

where (r_0, ϕ_0, θ_0) is the initial condition in the transformed coordinates and $t_{f2} = r_0(3\pi/2 - \phi_0)$. It should be noted that (13) reveals that the evolution of IC is a uniform circular motion with radius r_0, which is tangent to the x-axis of $\boldsymbol{\mathcal{F}}_i$ at the origin. Therefore, the tangent vector of IC at the origin is also $\boldsymbol{e}_x^i$. After t_{f2}, the IC stays at the origin since the singular point of $\mathbf{F}$ is also an equilibrium for the dynamics $\dot{\boldsymbol{p}} = \mathbf{F}(\boldsymbol{p})$.

• Case 2: $\boldsymbol{p}_0 \in \mathcal{R}_1 \backslash \mathcal{S}_1$.

The IC starting in $\mathcal{R}_1 \backslash \mathcal{S}_1$ consists two segments. The first segment within $\mathcal{R}_1$ is specified in the following while the second can be considered as a special case of (13). Firstly, define new coordinates (r, ϕ, θ) slightly different from (12)

$$x = r\cos\phi, \tag{14a}$$
$$y = (r\sin\phi + 2\rho)\cos\theta, \tag{14b}$$
$$z = (r\sin\phi + 2\rho)\sin\theta, \tag{14c}$$

where the positively invariant manifold Σ_{ab} is specified by $\theta = \mathrm{atan2}(-a, b)$ and the basis along (r, ϕ, θ) can be obtained by [24]:

$$[\boldsymbol{e}_r\ \boldsymbol{e}_\phi\ \boldsymbol{e}_\theta] = [\boldsymbol{e}_x\ \boldsymbol{e}_y\ \boldsymbol{e}_z]\boldsymbol{R}_1(\theta)\boldsymbol{R}_3(\phi), \tag{15}$$

with $\boldsymbol{R}_1(\cdot)$ and $\boldsymbol{R}_3(\cdot)$ being the rotation matrices about x- and z- axes, respectively. Therefore, the relationship between IC and VF in $\mathcal{R}_1$ can be written as

$$\mathbf{F} = F_r\boldsymbol{e}_r + F_\phi\boldsymbol{e}_\phi + F_\theta\boldsymbol{e}_\theta, \tag{16a}$$
$$\frac{\mathrm{d}r}{\mathrm{d}t} = F_r,\ r\frac{\mathrm{d}\phi}{\mathrm{d}t} = F_\phi,\ r\frac{\mathrm{d}\theta}{\mathrm{d}t} = F_\theta, \tag{16b}$$

where $F_r = \sqrt{4\rho^2 - r^2}/(2\rho)$, $F_\phi = r/(2\rho)$ and $F_\theta = 0$, referring to (7). Integrating (16b) with initial condition (r_0, ϕ_0, θ_0) gives

$$r(t) = 2\rho\cos(\phi_1 - \phi(t)), \phi(t) = \frac{t}{2\rho} + \phi_0, \theta(t) = \theta_0, \forall t < t_{f1}, \tag{17}$$

where $t_{f1} = 2\rho(\phi_1 - \phi_0)$ and $\phi_1 = \phi_0 + \arccos(r_0/(2\rho))$. Equation (17) shows that the IC is a circular arc with radius ρ, starting from (r_0, ϕ_0, θ_0) and ending at $(2\rho, \phi_1, \theta_0)$ in the coordinates given in (14). Additionally, denote the point specified by $(2\rho, \phi_1, \theta_0)$ as $\boldsymbol{p}_1$. It can be seen that $\boldsymbol{p}_1 \in \partial\mathcal{R}_1 \subseteq \mathcal{R}_2$, which implies that the IC enters $\mathcal{R}_2$ while being tangent to $\partial\mathcal{R}_1$ at time $t = t_{f1}$. Since the transformations (12) and (14) are equivalent on $\partial\mathcal{R}_1$, the second segment can be obtained by plugging $(2\rho, \phi_1, \theta_0)$ as the initial condition into (13). Then we have that

$$r(t) = 2\rho,\ \phi(t) = \frac{t}{2\rho} + \phi_1,\ \theta(t) = \theta_0,\ \forall t_{f1} \leqslant t \leqslant t_{f1} + t_{f2}, \tag{18}$$

where $t_{f2} = 2\rho(3\pi/2 - \phi_1)$. Equation (18) implies that the IC in this case arrives at the origin alone $\boldsymbol{e}_x^i$. After the arrival at the origin, the IC in Case 2 stays at the origin as in Case 1.

3) Given (13), (17) and (18), it becomes obvious that the ICs of $\mathbf{F}$ are of bounded curvature. For (13) and (18), there are $\kappa = 1/r_0 \leqslant 1/(2\rho) < \kappa_{max}$. While the curvature of (17) is given by $\kappa = 1/\rho = \kappa_{max}$. As for the trivial situation where $\boldsymbol{p}_0 \in \chi_- \cup \chi_+$, the IC is a straight line evolving on the x-axis and thus is of zero curvature. □

So far, the curvature-constrained VF $\mathbf{F}$ with origin and $\boldsymbol{e}_x^i$ as the desired position and the heading direction is presented. To arbitrarily specify $\boldsymbol{p}_d$ and $\boldsymbol{e}_d$ as suggested by (4a) and (4b), we propose the following corollary.

Corollary 1. *For $\mathbf{F}_d(\boldsymbol{p}) = \boldsymbol{R}_d\mathbf{F}(\boldsymbol{R}_d^{-1}(\boldsymbol{p} - \boldsymbol{p}_d))$, which is also continuous almost everywhere, the ICs converge to $\boldsymbol{p}_d$ along $\boldsymbol{e}_d = \boldsymbol{R}_d\boldsymbol{e}_x^i$ with curvature no larger than κ_{max} except for initial positions in the non-converging set $\mathcal{N}_d = \{\boldsymbol{p} \mid \boldsymbol{R}_d^{-1}(\boldsymbol{p} - \boldsymbol{p}_d) \in \chi_+ \bigcup \mathcal{S}\}$.*

Proof. The transformation from $\mathbf{F}$ to $\mathbf{F}_d$ is a composition of translation and rotation. Under such transformation, the attractor for dynamics $\dot{\boldsymbol{p}} = \mathbf{F}_d(\boldsymbol{p})$ is translated to $\boldsymbol{p}_d$ and the the tangent vector of IC approaching $\boldsymbol{p}_d$ is rotated to $\boldsymbol{e}_d$. The singular point set for $\mathbf{F}_d$ is specified by $\mathcal{S}_d = \{\boldsymbol{p} \mid \boldsymbol{R}_d^{-1}(\boldsymbol{p} - \boldsymbol{p}_d) \in \mathcal{S}\}$, which is still a lower dimensional manifold w.r.t. $\mathbb{R}^3$. Therefore, the transformed VF is also continuous almost everywhere. Similarly, the non-converging set $\mathcal{N}_d$ after the transformation is also a lower dimensional manifold, implying the almost global convergence of $\dot{\boldsymbol{p}} = \mathbf{F}_d(\boldsymbol{p})$ towards $\boldsymbol{p}_d$ along $\boldsymbol{e}_d$. Since the composition of translation and rotation is a positive isometry that preserves the curvature properties [25], we know that $\mathbf{F}_d$ is also curvature-constrained. □

IV. Controller Design

Theorem 1 and Corollary 1 together have defined the VF whose ICs are curvature-bounded and are attracted to the desired position $\boldsymbol{p}_d$ along $\boldsymbol{e}_d$. It is natural to come up with the idea of aligning the robot's velocity with the VF such that the robot can move along the IC and eventually achieve $\boldsymbol{p}_d$ with heading direction $\boldsymbol{e}_d$. Since the VF has only specified the expected orientation of $\boldsymbol{e}_x^b$ in $\boldsymbol{\mathcal{F}}_i$, we can take the Frenet-Serret frame of IC as the expected orientation of $\boldsymbol{\mathcal{F}}_b$. Therefore, we define the reference attitude by

$$\boldsymbol{R}_r = [\boldsymbol{T}\ \boldsymbol{N}\ \boldsymbol{B}] \in \mathrm{SO}(3). \tag{19}$$

In (19), the IC's tangent vector $\boldsymbol{T} = \mathbf{F}_d$ is determined by the proposed VF. Enlightened by Lemma 1, the binormal vector perpendicular to the positively invariant plane of $\mathbf{F}_d$ is given by $\boldsymbol{B} = \boldsymbol{e}_d \times (\boldsymbol{p} - \boldsymbol{p}_d)/\|\boldsymbol{e}_d \times (\boldsymbol{p} - \boldsymbol{p}_d)\|$ and the normal vector is $\boldsymbol{N} = \boldsymbol{B} \times \boldsymbol{T}$.

It is noticeable that when the robot's actual attitude $\boldsymbol{R}$ tracks the reference attitude $\boldsymbol{R}_r$, the attitude tracking error defined as $\boldsymbol{R}_e = \boldsymbol{R}_r^{-1}\boldsymbol{R}$ is stabilized to the identity matrix $\boldsymbol{I}$. When $\boldsymbol{R}_e$ is stabilized, $\boldsymbol{e}_x^b$ aligns with $\mathbf{F}_d$ and hence the robot moves along the IC of $\mathbf{F}_d$, eventually arriving at $\boldsymbol{p}_d$ in the direction of $\boldsymbol{e}_d$. Aiming to stabilize $\boldsymbol{R}_e$ in a finite time, the attitude control law is proposed in the following lemma.

Lemma 2. *Under the attitude control law*

$$\Omega^\wedge = -k_\omega\dot{\tau}\log_{\mathrm{SO}(3)}(\boldsymbol{R}_e) + \boldsymbol{R}^{-1}\dot{\boldsymbol{R}}_r\boldsymbol{R}_r^{-1}\boldsymbol{R}, \tag{20}$$

the attitude tracking error $\boldsymbol{R}_e$ is stabilized in a specified finite time T for any initial attitude $\boldsymbol{R}(0) = \boldsymbol{R}_0 \in \mathrm{SO}(3)$ such that $\mathrm{trace}(\boldsymbol{R}_e(0)) \neq -1$, where $\tau = \ln\frac{T}{T-t}$ is the time scaling function, $\log_{\mathrm{SO}(3)}$ is the logarithmic map on $\mathrm{SO}(3)$ and $k_\omega > 0$ is a scalar gain.

Proof. Referring to [15, Lemma 4], the proof of this lemma becomes a first-order special case of [26]. □

During the stabilization process of $\boldsymbol{R}_e$, the actual trajectory of robot still possibly differs from the IC and measures should be taken to ensure the curvature constraint is not violated. In response to this concern, an appropriate linear velocity control law is proposed as follows.

Lemma 3. *For $t \in [0, T)$, the linear velocity control law is*

$$v_x = k_v \sqrt{\Omega_y^2 + \Omega_z^2} + v_{min}, \tag{21}$$

where $k_v \geqslant 1/\kappa_{max}$ is the scalar gain and $v_{min} > 0$ is the speed lower bound. Then, the curvature of nonholonomic robot's trajectory is guaranteed to be $\kappa < \kappa_{max}$.

Proof. The proof is completed by plugging (21) into (3) $\square$

Let $\boldsymbol{p}_T$ and v_T denote the position and the linear velocity at time $t = T$, respectively. When $\boldsymbol{R}_e$ is stabilized, the attitude control law (20) is reduced to

$$\Omega^\wedge = \boldsymbol{R}^{-1} \dot{\boldsymbol{R}}_r \boldsymbol{R}_r^{-1} \boldsymbol{R}, \tag{22}$$

and the linear velocity control law is redesigned by

$$v_x = v_T \frac{\|\boldsymbol{p} - \boldsymbol{p}_d\|}{\|\boldsymbol{p}_T - \boldsymbol{p}_d\|}. \tag{23}$$

Under (22) and (23), the robot converges to $\boldsymbol{p}_d$ along $\boldsymbol{e}_d$ by following the IC of $\mathbf{F}_d$ from $\boldsymbol{p}_T$ to $\boldsymbol{p}_d$ under continuous control inputs. The control laws for curvature-constrained motion planning of nonholonomic robots are summarized in the following theorem.

Theorem 2. *Driven by control laws* (20)*,* (21) *on time interval $t \in [0\ T)$ and* (22)*,* (23) *for $t \geqslant T$, the trajectory of the closed-loop nonholonomic robot satisfies motion planning objectives in* (4)*, for any initial position $\boldsymbol{p}_0 \in \mathbb{R}^3 \backslash \mathcal{N}_d$ and initial attitude $\boldsymbol{R}_0 \in \mathrm{SO}(3)$ such that $\mathrm{trace}(\boldsymbol{R}_e(0)) \neq -1$.*

Proof. Under the attitude control laws (20) and (22), there is $\boldsymbol{R}_e(t) = \boldsymbol{I}$, $\forall t \geqslant T$ according to Lemma 2, meaning that the robot's velocity aligns with $\mathbf{F}_d$. According to [23], we know that the trajectory of robot follows the same geometric path of $\mathcal{I}(t - T, \boldsymbol{p}_T)$ on $t \geqslant T$, which is the IC of $\mathbf{F}_d$, starting from $\boldsymbol{p}_T$ and arriving at $\boldsymbol{p}_d$ along $\boldsymbol{e}_d$.

On the time interval $[0, T)$, Lemma 3 indicates that the trajectory curvature is bounded by κ_{max}. As for $t \geqslant T$, the trajectory of robot overlaps with the IC and hence is of curvature no larger than κ_{max}, referring to Corollary 1.

To show the convergence of position, we assume that the robot converges to $\boldsymbol{p}'_d \in \{\mathcal{I}(t - T, \boldsymbol{p}_T) \mid t \geqslant T\}$ and $\boldsymbol{p}'_d \neq \boldsymbol{p}_d$. To achieve convergence, there should be $\dot{\boldsymbol{p}} = 0$ at $\boldsymbol{p}'_d$. However, according to (23), $\dot{\boldsymbol{p}} = 0$ if and only if $\boldsymbol{p} = \boldsymbol{p}_d$. Since the points on the IC forms a closed set according to the proof of Theorem 1, the robot converges to $\boldsymbol{p}_d$, i.e., (4a) is satisfied. Furthermore, based on Corollary 1, there hold (4b) and (4c) for initial condition $\boldsymbol{p}_0 \in \mathbb{R}^3 \backslash \mathcal{N}_d$ and $\boldsymbol{R}_0 \in \mathrm{SO}(3)$ such that $\mathrm{trace}(\boldsymbol{R}_e(0)) \neq -1$. $\square$

V. Numerical Simulation Results

To verify the effectiveness of the proposed algorithm, several simulation cases with different initial conditions are conducted in two examples. For each case in Example 1, the nonholonomic robot starts from $\mathcal{R}_1$ while the desired position and heading direction are specified by $\boldsymbol{p}_d = [3, 6, 9]^{\mathrm{T}}$ and $\boldsymbol{e}_d = [\frac{1}{2}, \frac{1}{2}, \frac{\sqrt{2}}{2}]^{\mathrm{T}}$. As for Example 2, the initial conditions lie in $\mathcal{R}_2$ and $\boldsymbol{p}_d = [-15, 5, -10]^{\mathrm{T}}$, $\boldsymbol{e}_d = [\frac{3}{4}, -\frac{\sqrt{3}}{4}, -\frac{1}{2}]^{\mathrm{T}}$. The maximum curvature is set as $\kappa_{max} = 0.2$ in both examples. The initial attitude of the robot is depicted by roll-pitch-yaw Euler angles denoted as $\alpha_0, \beta_0, \gamma_0$ and the initial conditions are given in Table I where the Euler angles are in radian.

The trajectories and state evolution of simulation results are presented in Figures 2 and 3, respectively. The curves in Figures 3 and 4 use the same colors as the icons in Figure 2 for each case. In the attitude evolution of Figure 3, we show components of the heading direction $\boldsymbol{e}_x^b = [R_{11}, R_{21}, R_{31}]^{\mathrm{T}}$ in accordance with motion planning objective (4b). These results indicate the satisfaction of objectives (4a) and (4b), i.e., robots with distinct initial conditions all converge to the desired position with specified heading direction. Figure 4 shows the trajectory curvature κ and relevant control inputs w.r.t. time while κ_{max} is illustrated by red dotted line. It is obvious that the curvature constraint (4c) is guaranteed under the proposed algorithm. Moreover, the curvature converges to a constant value in each case, which verifies the fact that each segment of IC in $\mathcal{R}_1$ and $\mathcal{R}_2$ has constant curvature.

TABLE I
Initial Conditions of Different Cases.

		Initial position			Initial attitude		
		x_0	y_0	z_0	α_0	β_0	γ_0
Example 1	Case 1	-5.8	12.2	22.2	2.6	-0.4	3.1
	Case 2	8.2	-0.5	19.8	2.4	-0.8	-2.4
	Case 3	13.1	7.7	9.1	-3.0	-0.5	0.5
	Case 4	4.8	12.8	10.0	-2.2	-0.9	1.2
Example 2	Case 1	10.9	-4.2	-3.3	2.7	-0.2	0.7
	Case 2	-10.4	-19.7	-13.3	-2.1	0.9	-1.3
	Case 3	-16.9	0.2	-32.7	-2.8	0.6	-0.3
	Case 4	1.4	17.8	-23.7	1.2	-2.2	1.9

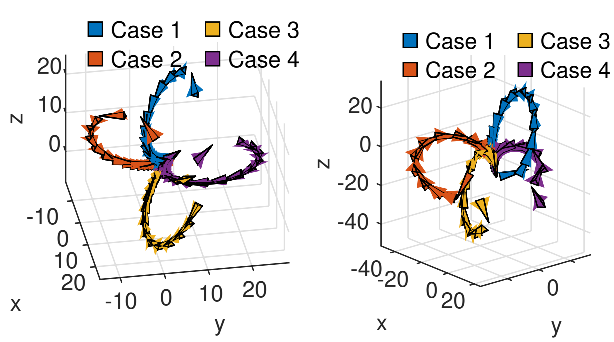

(a) Example 1 (b) Example 2

Fig. 2. Trajectories in different examples

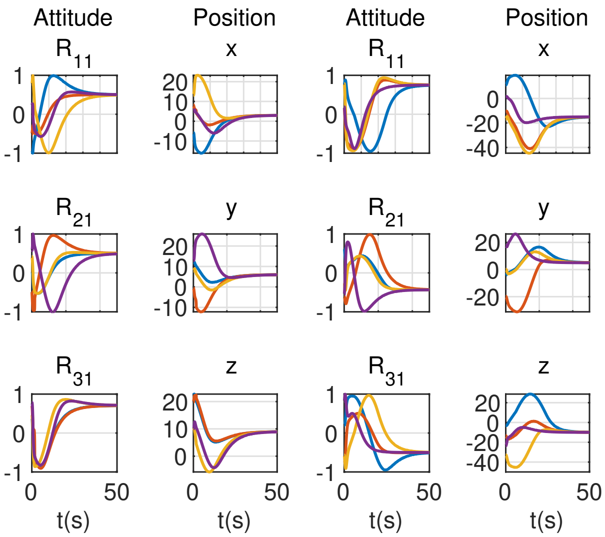

(a) Example 1 (b) Example 2

Fig. 3. State evolution in different examples

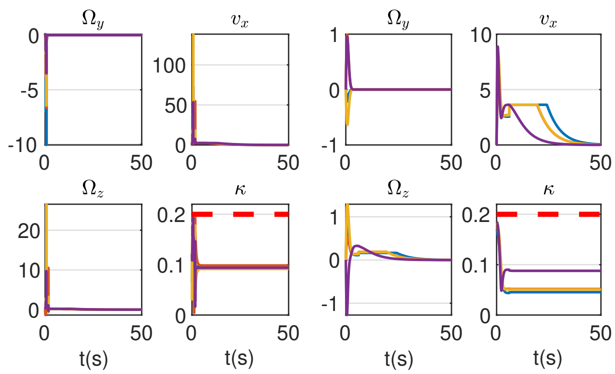

(a) Example 1 (b) Example 2

Fig. 4. Curvature and relevant control inputs, κ_{max} presented by red dotted line

VI. Conclusions

This paper has proposed a motion planning algorithm based on a curvature-constrained vector field for 3D nonholonomic robots, whose trajectories are subject to upper bounded curvature. The integral curves of proposed vector field satisfy the curvature constraint and are almost globally attracted to the desired position with a specified heading direction. Furthermore, the attitude and linear velocity control laws are designed, under which the nonholonomic robot can track the integral curve of the vector field in a finite time and converge to the desired states. Future research will investigate smooth VF for better control performance and consider more complex scenarios such as input saturation, obstacle and collision avoidance under the curvature constraint.

References

[1] S. M. LaValle, *Planning algorithms*. New York, NY, USA: Cambridge University Press, 2006.

[2] Z. Liu, M. Guo, W. Bao, and Z. Li, "Fast and adaptive multi-agent planning under collaborative temporal logic tasks via poset products," *Research*, vol. 7, p. 0337, 2024.

[3] S. Li and X. Wang, "Finite-time consensus and collision avoidance control algorithms for multiple AUVs," *Automatica*, vol. 49, no. 11, pp. 3359–3367, 2013.

[4] X. He, Z. Li, X. Wang, and Z. Geng, "Roto-translation invariant formation of fixed-wing UAVs in 3D: Feasibility and control," *Automatica*, vol. 161, p. 111492, 2024.

[5] M. Kallman and M. Mataric, "Motion planning using dynamic roadmaps," in *IEEE International Conference on Robotics and Automation*, 2004, pp. 4399–4404.

[6] L. Zhang, Y. J. Kim, and D. Manocha, "A hybrid approach for complete motion planning," in *IEEE/RSJ International Conference on Intelligent Robots and Systems*, 2007, pp. 7–14.

[7] S. Karaman and E. Frazzoli, "Sampling-based algorithms for optimal motion planning," *The International Journal of Robotics Research*, vol. 30, no. 7, pp. 846–894, 2011.

[8] R. M. Murray and S. S. Sastry, "Nonholonomic motion planning: Steering using sinusoids," *IEEE Transactions on Automatic Control*, vol. 38, no. 5, pp. 700–716, 1993.

[9] I. I. Hussein and A. M. Bloch, "Optimal control of underactuated nonholonomic mechanical systems," *IEEE Transactions on Automatic Control*, vol. 53, no. 3, pp. 668–682, 2008.

[10] O. Khatib, "Real-time obstacle avoidance for manipulators and mobile robots," *The International Journal of Robotics Research*, vol. 5, no. 1, pp. 90–98, 1986.

[11] C. I. Connolly, J. B. Burns, and R. Weiss, "Path planning using laplace's equation," in *IEEE International Conference on Robotics and Automation*, 1990, pp. 2102–2106.

[12] D. E. Koditschek and E. Rimon, "Robot navigation functions on manifolds with boundary," *Advances in Applied Mathematics*, vol. 11, no. 4, pp. 412–442, 1990.

[13] S. R. Lindemann and S. M. LaValle, "Simple and efficient algorithms for computing smooth, collision-free feedback laws over given cell decompositions," *The International Journal of Robotics Research*, vol. 28, no. 5, pp. 600–621, 2009.

[14] D. Panagou, "A distributed feedback motion planning protocol for multiple unicycle agents of different classes," *IEEE Transactions on Automatic Control*, vol. 62, no. 3, pp. 1178–1193, 2017.

[15] X. He, W. Yao, Z. Sun, and Z. Li, "A novel vector-field-based motion planning algorithm for 3D nonholonomic robots," 2023, arXiv:2302.11110.

[16] X. He and Z. Li, "Simultaneous position and orientation planning of nonholonomic multi-robot systems: A dynamic vector field approach," *IEEE Transactions on Automatic Control*, 2024, doi: 10.1109/TAC.2024.3406475.

[17] L. E. Dubins, "On curves of minimal length with a constraint on average curvature, and with prescribed initial and terminal positions and tangents," *American Journal of mathematics*, vol. 79, no. 3, pp. 497–516, 1957.

[18] M. Hwangbo, J. Kuffner, and T. Kanade, "Efficient two-phase 3D motion planning for small fixed-wing UAVs," in *IEEE International Conference on Robotics and Automation*, 2007, pp. 1035–1041.

[19] H. Chitsaz and S. M. LaValle, "Time-optimal paths for a Dubins airplane," in *IEEE Conference on Decision and Control*, 2007, pp. 2379–2384.

[20] D. Lau, J. Eden, and D. Oetomo, "Fluid motion planner for nonholonomic 3-D mobile robots with kinematic constraints," *IEEE Transactions on Robotics*, vol. 31, no. 6, pp. 1537–1547, 2015.

[21] A. Marchidan and E. Bakolas, "A local reactive steering law for 2D collision avoidance with curvature constraints and constant speed," *Robotics and Autonomous Systems*, vol. 155, p. 104156, 2022.

[22] J. Stewart, "Continuity," in *Calculus*, 7th ed. Boston, MA, USA: Cengage Learning, 2011, ch. 1.8, pp. 81–93.

[23] C. Chicone, "Reparametrization of time," in *Ordinary differential equations with applications*, 2nd ed. New York, NY, USA: Springer Science & Business Media, 2006, ch. 1.5, pp. 16–20.

[24] K. S. Surana, "Appendix B: Transformations and operations in cartesian, cylindrical and spherical coordinate systems," in *Advanced Mechanics of Continua*. Boca Raton, FL, USA: CRC Press, 2014, pp. 705–719.

[25] T. F. Banchoff and S. Lovett, "Curves in space: Local properties," in *Differential geometry of curves and surfaces*, 2nd ed. Boca Raton, FL, USA: CRC Press, 2016, ch. 3.4, pp. 97–101.

[26] X. Peng, J. Sun, and Z. Geng, "A specified-time control framework for control-affine systems and rigid bodies: A time-rescaling approach," *International Journal of Robust and Nonlinear Control*, vol. 29, no. 10, pp. 3163–3182, 2019.